Ultrafast probes of photovoltage and two-dimensional electron gas in the topological insulator Bi₂Te₃ by angle-resolved photoemission and terahertz spectroscopy

Bumjoo Lee [1,2] Yukiaki Ishida,[1,3] Jonghyeon Kim [4] Jinsu Kim,[5,*] Na Hyun Jo,[5,6] So Yeun Kim,[1,2,†] Inho Kwak [1,2]
Min-Cheol Lee [1,2] Kyungwan Kim [7] Jae Hoon Kim [4] Myung-Hwa Jung [5] Shik Shin,[3]
Tae Won Noh,[1,2] and Hyunyong Choi [2,8,‡]

[1]*Center for Correlated Electron Systems, Institute for Basic Science, Seoul 08826, Republic of Korea*
[2]*Department of Physics and Astronomy, Seoul National University, Seoul 08826, Republic of Korea*
[3]*Institute for Solid State Physics, The University of Tokyo, Kashiwa, Chiba 277-8581, Japan*
[4]*Department of Physics, Yonsei University, Seoul 03722, Republic of Korea*
[5]*Department of Physics, Sogang University, Seoul 04107, Republic of Korea*
[6]*Department of Physics, University of Michigan, Ann Arbor, Michigan 48109, USA*
[7]*Department of Physics, Chungbuk National University, Cheongju 28644, Republic of Korea*
[8]*Institute of Applied Physics, Seoul National University, Seoul 08826, Republic of Korea*

Photoexcited carriers in three-dimensional topological insulators (3D TIs) decay rapidly through the electron-electron and electron-phonon scattering. While most studies focus on such fast dynamics, recent experiments find the slow photovoltage (PV) dynamics arising from the band-bending potentials, in which the optical transitions in two-dimensional electron gas (2DEG) are effective. Although early investigations speculated the existence of multiple band-bending structures from the TI surface to the TI bulk, how PV and 2DEG are correlated in the presence of such multiple band bendings has been less explored. Here, we employ the combination of time- and angle-resolved photoemission spectroscopy (tr-ARPES) and ultrafast time-resolved terahertz (tr-THz) spectroscopy to investigate the PV and 2DEG dynamics in the prototypical topological insulator Bi₂Te₃. Our tr-ARPES analysis identifies two spatially separated PV dynamics associated with two types of band bending: one is the well-known surface PV, and another PV is formed deep within the bulk, which we call "internal bulk PV." For the surface PV, our tr-THz spectra substantiate that the μs-long transient signal arises from the surface-PV-induced increase of the TSS and 2DEG carrier density, which appears as a transient blueshift of a Fermi cutoff and an increased ARPES intensity in the tr-ARPES measurements. In contrast, the effect of the internal bulk PV shows only marginal changes in the 2DEG and TSS carrier densities but shifts the entire binding energy of the near-surface bands.

The Dirac fermions in three-dimensional topological insulators (3D TIs) exhibit unusual electronic and optical properties, stemming from topologically protected metallic surface states. Carriers in the topological surface state (TSS) exhibit interesting transport properties due to linear energy-momentum dispersion [1,2], including helical spin texture [3] and ultrahigh carrier mobilities [3] in the absence of magnetic impurities. The proximity effect of TIs and other materials can give rise to complex electronic states. Remarkable discoveries include the possibility of observing Majorana bound states [4], unconventional topological magnetoelectric effect [5], and nonlinear effects [6]. On an optical side, the helical spin texture and time-reversal symmetry give rise to interesting photoinduced phenomena: experiments using circularly

polarized optical excitation show the spin-polarized current [7,8], band-gap opening at the Dirac point [9], and helicity-dependent photocurrent [10].

Such phenomena arise from the helical Dirac fermions on the TSS, a fundamental low-energy excitation of bulk-insulating TIs. However, the TSS is not the only origin of the surface phenomena in TIs [1,11]. The inhomogeneous charge density between the TSS and the bulk state [12] results in a spatially modulated electrostatic potential, whose variation extends from the surface to the deep down in the bulk [11,13–18]. The photoexcited electron and hole pairs are spatially separated due to such potentials, where the recombination rate becomes significantly different depending on the spatial photocarrier distribution [14,15,17]. As a result, the residual photoconductivity can be present in a few-μs time scale, dominating the transient electronic and optical characteristics [19–21].

Understanding such effects is important because it is known that a large density of photoexcited carriers is relaxed in ultrafast time scales of around a few ps, yet "slow" electrostatic kinetics, which typically occurs in a few 100's of

---

*Present address: Physical Engineering Division, Busan Institute, National Forensic Service, Yangsan 50612, Korea.

†Present address: Department of Physics, University of Illinois at Urbana-Champaign, Urbana, 61801 IL, USA.

‡Corresponding author: hy.choi@snu.ac.kr

ps or longer, further activates the charge accumulation due to the band bending [11,14–17]. It is well established that the former "fast" dynamics inject the bulk carriers into the TSS, whereby a rapid relaxation of Dirac fermions takes place near the TI surfaces [19,22,23]. On the other hand, the latter slow kinetics are less explored, where the relaxed carriers are known to be redistributed spatially until the equilibrium state reaches [11,13–17]. Following the conventional electrostatics of the metal-semiconductor junction [11], it has been recognized from early reports that the band-bending direction is determined from the majority carrier type of the bulk, where the "upward" band bending is known to be favorable for the *n*-type TIs [11,14–17]. But two-dimensional electron gas (2DEG), which requires "downward" band bending, is often found even for the heavily *n*-doped TIs [24–27]. Numerous surface-sensitive angle-resolved photoemission spectroscopy (ARPES) measurements were conducted in a series of different conditions of samples, such as controlled band bending via chemical methods [15], electrostatic control [26], or temperature [16]. However, it has remained elusive to explain the effects of the time-resolved photocarrier dynamics and the existence of quantum confinement [18,24–27] on the band bending that satisfies such conventional electrostatics [11,15,17].

In this study, we perform time-resolved angle-resolved photoemission spectroscopy (tr-ARPES) and time-resolved THz (tr-THz) spectroscopy in *n*-type Bi_2Te_3 3D TI single crystals. Our investigation has found that two types of bend bending coexist, where the associated photocarrier distributions and photovoltages (PVs) are strongly time dependent. The left panel in Fig. 1(a) is the schematic diagram of our experiment. Our aim in this study is to investigate the effect of such PV dynamics on the composite band bending as well as on the photocarrier dynamics near TSS and 2DEG [the right panel in Fig. 1(a)]. There are the following motivations for employing two ultrafast spectroscopies. First, the time- and angle-resolved ARPES is the primary tool to investigate the PV dynamics [9,14–16,28]. However, these measurements are not sensitive to the low-energy transition occurring in a meV scale [29], such as carrier dynamics within the quantized 2DEG subbands [30]. Second, ultrafast THz spectroscopy can overcome this limitation in investigating the low-energy optical conductivity. THz spectroscopy provides additional perspectives for probing the low-energy electromagnetic transitions of the TI Dirac fermions [30,31].

The Bi_2Te_3 single crystal is synthesized by the Bridgeman method [32]. To compensate for the loss of Te during the synthesis, we have mixed the Bi and Te powders with the composition of 2:3.06. The mixture was melted at a soaking temperature of 800 °C for 16 h, slowly cooled to 550C, kept for three days at 550 °C, and then finally cooled to room temperature [32]. The Bi_2Te_3 crystal tends to have an *n*-type majority carrier arising from the antisite defects of type Te_{Bi} [33]. In our sample growth condition, the *n*-type carrier was identified by the Hall measurement [33]. For the optical pump excitation, the 800-nm, 40-fs pump pulses were delivered from a Ti:sapphire 250-kHz regenerative amplifier (Coherent® RegA 9040, see Supplemental Material S1 for the measurement details [34]). The equilibrium and the time-dependent band structure were obtained by ARPES and
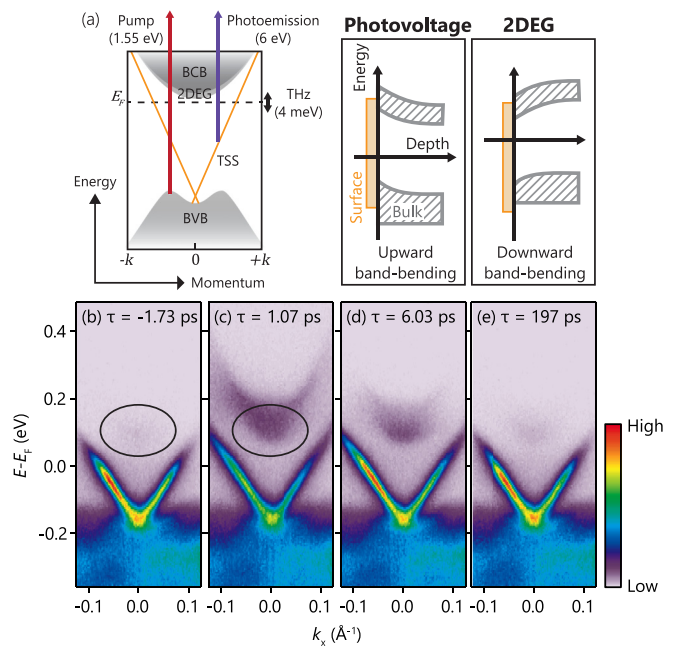

FIG. 1. (a) Schematic illustration of our experiment and the band structure. The time-dependent changes of the upward band bending in *n*-type TI are associated with the PV dynamics. On the contrary, prior reports on the two-dimensional electron gas (2DEG) require a downward band bending, which is related to the surface PV. (b)–(e) Time-dependent band structure dynamics measured by tr-ARPES. Each panel represents the tr-ARPES image recorded at different pump-probe delay τ. (b) On top of the linear dispersion of the topological surface state (TSS), a small contribution from the quadratic band was observed at delay $\tau = -1.73$ ps (black circle). After the arrival of the pump pulse (c)–(e), the quadratic band whose energy bottom is at $E - E_F \sim 0.1$ eV (black circle) becomes visible.

tr-ARPES, respectively. The employed ARPES spectrometer consists of a hemispherical analyzer [35], in which we used the 1.5 eV as the pump pulses and the frequency-quadrupled 5.9 eV as the probe pulses. We reduced the probe fluence to avoid the space-charge broadening effect until the photoemission spectra shift became less than 3 meV. The photoelectron energy E was calibrated using the Fermi cutoff level E_F of a gold contact, which was placed right next to the sample and grounded to the analyzer. The energy resolution was estimated to be ∼15 meV, which was obtained from the Fermi cutoff fit after convoluting the Fermi-Dirac function with a Gaussian function. All measurements were performed at 300 K, and all pump-probe measurements utilized the pump pulse with an absorbed fluence F of 10 μJ/cm^2.

Figures 1(b)–1(e) show the energy-momentum spectra measured at several pump-probe delays τ. At $\tau = -1.73$ ps, the probe pulse measures the occupied states before the pump arrival. The contribution of the quadratic band can be seen, although the ARPES intensity is weak (black circle). We have observed that the Dirac point is located at $E_D - E_F = -167$ meV with the TSS Fermi velocity v_F of 3.4×10^5 m/s. Immediately after the pump, the ARPES intensity of the occupied TSS bands ($E - E_F < 0$ eV) is reduced, and that of the quadratic band is enhanced (black circle), as shown in Fig. 1(c). Within a few picoseconds [Figs. 1(c) and 1(d)],

multiple contributions are involved, such as transient photo-carrier relaxation [36,37], bleaching [31], or diffusion [28], wherein prior studies have been extensively performed to identify each corresponding kinetics for the spectral signatures. After these rapid relaxation processes, the photoexcited changes become simpler than that of Fig. 1(d). We observe that the occupation of TSS and the quadratic band increases, as shown in Fig. 1(e).

To analyze the results further, we examine the energy distribution curve (EDC) of the tr-ARPES results. Figure 2(a) is EDC measured at $\tau = -1.73$ ps, showing a pronounced peak near the Dirac point (black arrow in the left panel) as well as the bottom of the quadratic band (red arrow in the right panel). Here, we note that the black arrow, i.e., the estimated binding energy of the Dirac point, is located slightly below the peak of ARPES intensity. This is because we have extrapolated the band dispersion near E_F to specify the location of the Dirac point by assuming a linear energy-momentum dispersion. This approach is useful when we calculate the carrier density from the ARPES spectrum because the carrier density can be estimated from the Fermi surface area at E_F. After the pump ($\tau = 1.07$ ps), Fig. 2(b) shows the reduced ARPES intensity in the occupied bands (bulk valance band and TSS, left panel) and the increased signal in the quadratic band above $E - E_F \sim 0.1$ eV (right panel). Compared to the data of Fig. 2(a) at τ of -1.73 ps, the ARPES intensity above $E - E_F \sim 0.1$ eV (right panel, red arrow) exhibits a strong time dependence. Because the density of the photoexcited electron and hole is directly associated with the PV effect [17,38], we have further performed the pump fluence F-dependent ARPES measurements. In Fig. 2(c), we compare the ARPES data with an equilibrium state. Here, the blue solid line is the case of no-pump excitation ($F = 0$ μJ/cm²). We see that the TSS binding energy (left panel) and the ARPES intensity of the quadratic band (right panel) are enhanced with increasing F. Considering that τ is negative ($\tau = -0.13$ ps), we attribute the origin of TSS binding energy shift to the long-lived PV in the upward band bending, whose effects are to enhance the TSS binding energy. We note that the EDC intensity shift near the Γ point directly represents the Dirac point shift. The EDC preserves its form at $\tau > 340$ ps, which indicates the rigid band shift of the TSS bands including the Dirac point and the bulk valence bands (BVBs) near the surface (see Supplemental Material S2 [34]). The quantitative amounts of the binding energy shifts ΔV_U were obtained by the following method. We first calculate the EDC intensity $I(E)$ near the Γ point with the pump excitation $I_1(E)$ and with no-pump excitation $I_2(E)$. Then, we find the value ΔV_U that minimizes $\sum_E [I_1(E) - I_2(E-\Delta V_U)]^2$. The iteration method for the calculation is equivalent to a least-square fitting, where the value and the corresponding confidence interval were obtained from the fitting and Jacobian matrix, respectively. For example, the TSS binding energy shift is positive with the magnitude ΔV_U of 5.5 ± 0.3 meV when F is 10 μJ/cm². The shift is calculated from the integrated intensities of the bands with broadening, where the energy resolution of the measurement setup does not limit the identification of the band shift. If the surface PV is the origin, then holes should be accumulated toward the surface due to the upward band-bending structure, which would push the Fermi cutoff near the Dirac
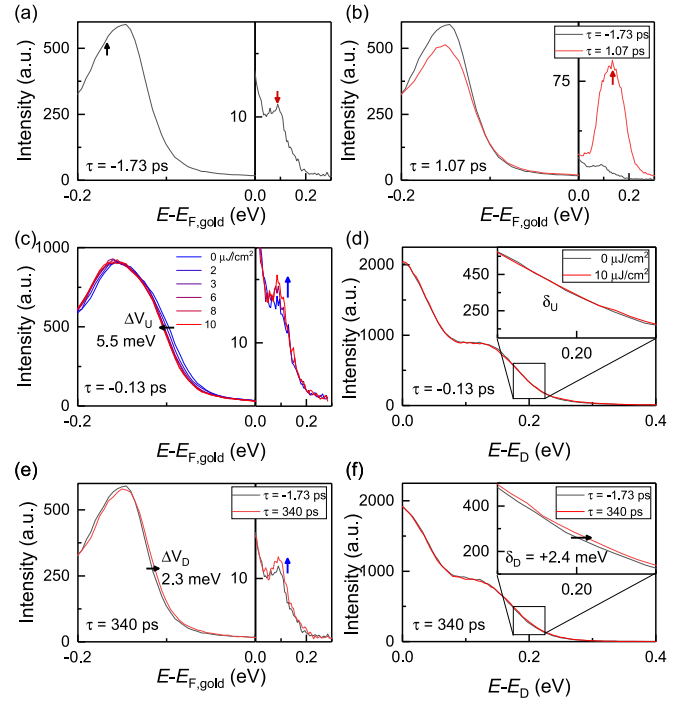

FIG. 2. The Dirac point and Fermi cutoff shift observed via tr-ARPES (a) Energy distribution curves (EDCs) near Γ point (integrated from -0.02 to 0.02 Å⁻¹) recorded at $\tau = -1.73$ ps. The black and red arrows indicate the peak of the Dirac point and the quadratic band, respectively. (b) EDC near Γ point measured at 1.07 ps (red solid line). For easy comparison, we show the data at $\tau = -1.73$ ps (black solid line) on top of it. After the pump arrival, the ARPES intensity in the unoccupied side ($E - E_F < 0$) is reduced while the intensity around $E - E_F \sim 0.1$ eV (red arrow) is enhanced. (c) The fluence (F) dependent EDC shift at the negative delay $\tau = -0.13$ ps. Compared to the equilibrium (no pump excitation, 0 μJ/cm²), the TSS binding energy is increased ($\Delta V_U > 0$) with increasing F (left panel). We attribute $\Delta V_U > 0$ to the internal bulk PV in the upward band bending. The blue arrow indicates the increased quadratic band in the ARPES intensity (right panel). (d) The Fermi cutoff shift relative to the Dirac point at a negative delay $\tau = -0.13$ ps. No Fermi cutoff shift was seen. (e) EDC near Γ point is shown at τ of -1.73 ps (black solid line) and 340 ps (red solid line). In contrast to (c), the reduced TSS binding energy $|\Delta V_D|$ of 2.3 meV is observed under the same F of 10 μJ/cm² (left panel). We attribute ($\Delta V_D < 0$) to the surface PV in the downward band bending. The blue arrow has the same meaning as the right panel of (c). (f) The Fermi cutoff shifts relative to the Dirac point at $\tau = -1.73$ ps (black solid line) and at 340 ps (red solid line). A positive Fermi cutoff shift δ_D of 2.4 meV is observed at $\tau = 340$ ps. Note that the relative shift was compared to the Dirac point energy.

point [15,17]. Here, we define the Fermi cutoff as the energy of the 50% occupancy probability that is visible on the surface. We have obtained that the photocarrier density changes δ_U were obtained by the same method to obtain ΔV_U. We calculate the EDC intensities on the whole measured degree range of with the pump excitation $I_1(E)$ and with no-pump excitation $I_2(E)$. Our result show $\Delta V_U + \delta_U = 5.9 \pm 0.4$ meV, which indicates negligible δ_U, as shown in Fig. 2(d). From the finite ΔV_U and negligible δ_U, we see that the observed rigid band shift is not explained by the surface PV [17]. We
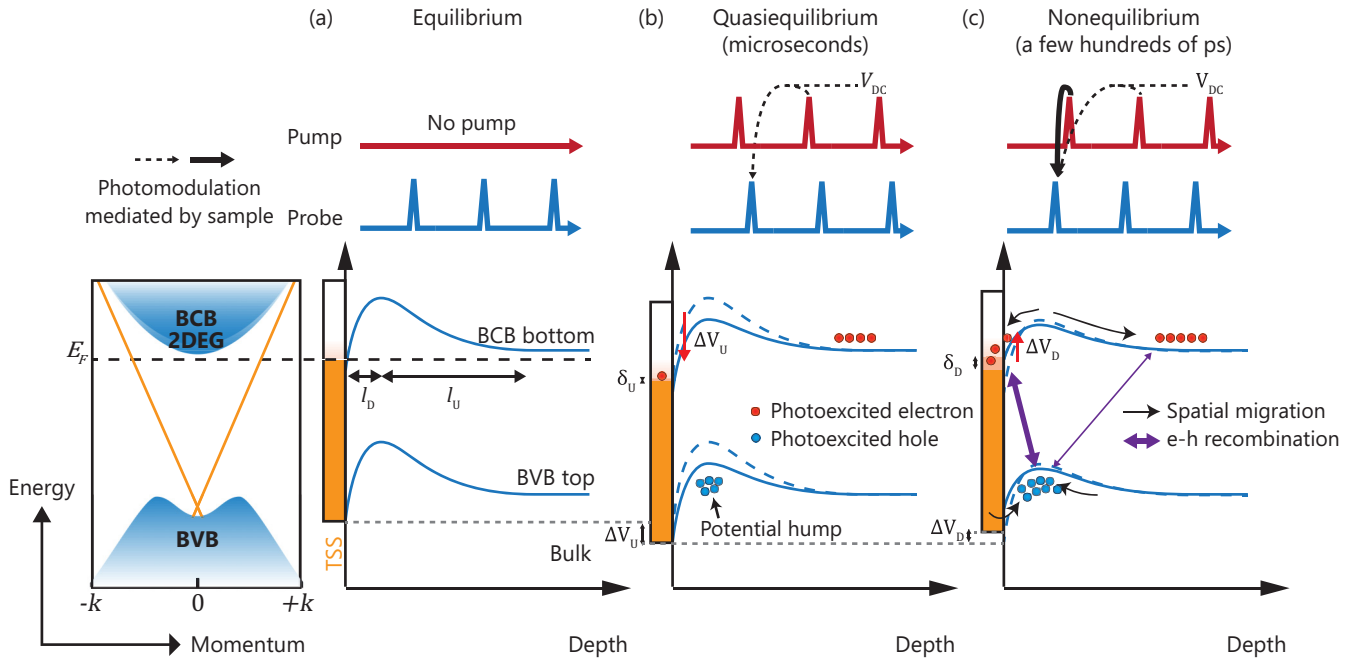
FIG. 3. Schematics of the band structure and the energy band diagram. (a) The energy band diagram (blue solid line) in an "equilibrium" state, i.e., no pump excitation. The energy level of Fermi cutoff E_F is indicated by black dotted lines. The bulk state is assumed to be an n-doped semiconductor. The spatial distance of the downward band bending (l_D) and the upward band bending (l_U) is indicated by the black bidirectional arrows. (b) Photocarrier distribution on top of the energy band diagram in a "quasiequilibrium" state at negative τ. The effect of the prepump pulses (4 μs ahead) is to build up the DC component of V_{DC}. The solid red dots indicate the photoexcited electrons and the blue solid dots are the photoexcited holes. The TSS binding energy is enhanced by the internal bulk PV (red arrow) compared to the no pump case. The energy band diagram of the quasiequilibrium (blue solid line) is compared to the equilibrium (blue dotted line). (c) The photocarrier dynamics at about a few hundreds of picoseconds. We call this energy band diagram a "nonequilibrium" one to distinguish this state from the other two states. The photoexcited carriers result in two spatially distinct PVs; one is the surface PV near TSS and another is the internal bulk PV occurring deep into the TI bulk. Both PVs reduce the band bending compared to the quasiequilibrium. The surface PV (red arrow) reduces the TSS band binding energy compared to the quasiequilibrium case. The purple arrows intend to describe the electron-hole recombination. Blue dotted lines are for the energy band diagram in the quasiequilibrium state, and blue solid ones are for the nonequilibrium state.

suggest that the band shift on the surface originates from the upward band bending buried below the measurable depth of ARPES [17].

In contrast to the above measurements, an intriguing observation is the relative reduction of TSS band binding energy at $\tau = 340$ ps. Figures 2(e) and 2(f) show the binding energy shifts of the TSS band and the Fermi cutoff at $\tau = 340$ ps relative to the measurement at $\tau = -1.73$ ps. In Fig. 2(e), we observe the negative binding energy shift of the TSS band by $\Delta V_D = 2.3 \pm 0.4$ meV. The sum of the Fermi cutoff shift δ_D and ΔV_D is 3.2 ± 0.6 meV, which indicates a positive δ_D as shown in Fig. 2(f). These observations indicate that electrons are accumulated near TSS, and the corresponding origin can be explained by the surface PV activated in the downward band bending [17].

The above tr-APRES data suggest that the band bending is not monotonic, but exhibits an interesting feature of two spatially and temporally separated PVs, each of which is in an opposite direction. To illustrate our results, we show in Fig. 3(a) a composite band-bending diagram where the downward (near the surface with a length of l_D) and upward (deep into the bulk with a length of l_U) band bending coexist. We propose how the composite band bending can explain our experimental results in the following. For the downward

band bending, the PV dynamics occur just beneath the TI surface, which can be understood by the surface PV effect. On the other hand, the PV dynamics associated with the upward band bending exhibit an opposite PV direction deep in the bulk, which we call "internal bulk PV" [39,40] to distinguish it from the surface PV. Supposing $l_D \ll l_U$, the measured time-dependent PV dynamics are explained as follows. At the negative τ, the pump pulse excites the sample before the 4 μs (the laser repetition period is 4 μs) of the probe pulse, where the quasiequilibrium state can be observed, as shown in Fig. 3(b). When τ is positive, the photoexcitation creates photocarriers on both band bending below and above l_D as displayed in Fig. 3(c). We separately denote the effect of the previous pump pulses as V_{DC}, which is shown in Fig. 3(b). Under the condition of $l_D \ll l_U$, because the photoexcited electrons below l_D (near the surface) are spatially closer to the photoexcited holes, the electrons and holes near the surface recombine faster than those in the bulk [14]. Consequently, although the quasi-E_F can change along the depth direction from the surface, the internal bulk PV effect dominates the photoinduced changes in the quasiequilibrium state for τ over 4 μs. In this case, the photoexcited electrons are accumulated deep in the bulk, and the photoexcited holes are accumulated near l_D.

We substantiate the above discussions by estimating the length scale of l_U and l_D. This comparison is important because the surface PV and internal bulk PV are time dependent, which would affect the transient carrier dynamics near the surface and deep into the bulk. The band-bending length l is related to the photoexcited charge carrier density Δn and the PV shift ΔV via $\Delta n e_0 = \epsilon \Delta V / l$ following a parallel capacitor model [17]. We suppose that the photoexcited carrier density is proportional to the absorbed pump photon density. Then, the relationship between l_U and l_D is given by

$$l_U = \Delta V_U / \Delta V_D (1 - e^{l_D/\delta_p}) l_D, \tag{1}$$

where δ_p is the penetration depth of the pump, which was determined to be $\delta_p = 15$ nm from the ellipsometry measurement [41] (see Supplemental Material S3 [34]). We estimate l_U to be at least 52 nm by solving a Poisson equation [11,42,43] (see Supplemental Material S4 [34]). Then, the calculated l_D is about 14 nm, where l_U is at least three times larger than l_D (see Supplementarl Material S4 [34]). Interestingly, the estimated l_D is consistent with the confinement potential length scale reported in previous 2DEG and surface PV studies [18,24,25,27]. Although the weak interlayer interaction might be another possibility to the origin of downward band bending, the van der Waals gap expansion of 1 or 2 quintuple layer (QL) [44] is too short to account for the band-bending length.

A natural consequence of such a short downward band bending is to confine the carriers near the surface that induces the Rashba-type spin split and the formation of 2DEG (see Supplemental Material S5 [34]) [24–27]. For a self-consistency check, we calculated the Rashba coupling parameter α using the ARPES intensity distribution curves. The Rashba coupling parameter α is proportional to the effective electric field [26] for the downward band bending, which is inversely proportional to l_D. To measure the Rashba-type band splitting, we focus on the tr-ARPES data $\tau = 1.07$ ps, where the 2DEG bands are clearly visible [45–48]. Figure 4(a) shows the momentum-distribution curve (MDC) at $E - E_F = 239.6$ meV displaying the split bands [49]. The band structures can be fitted using two Lorentz functions; the center wave vectors are 0.090 and 0.136 Å^{-1} with the same spectral width of 0.044 Å^{-1}. To estimate α, we use the following dispersion [26,50,51]:

$$E^{\pm}(k) = E_0 + \frac{\hbar^2 k^2}{2m^*} \pm \alpha k, \tag{2}$$

where m^* is the effective carrier mass and α is the Rashba coupling parameter. The fit of EDC at $k = 0$ shows that the binding-energy centers of the quadratic bands at $E_0 - E_F$ are 121 and 167 meV [Fig. 4(b)]. We obtain $\alpha = 0.45$ Å eV from the fitting results to the MDC and EDC data, which is similar to the value of 0.36 Å eV obtained by King *et al.* [26] (see Supplemental Material S5 for simulations on the Rashba coupling parameters [34]). The origin may be due to the adsorption of the adatom, for example, CO or H_2O that is common even in the ultrahigh vacuum [26,52]; the adsorption of the adatoms on TIs then results in the downward band bending of a short length scale (up to $\sim$20 nm) and a large energy scale ($\sim$200 meV) [24–27], where the quantized 2DEG can be resolved [49].
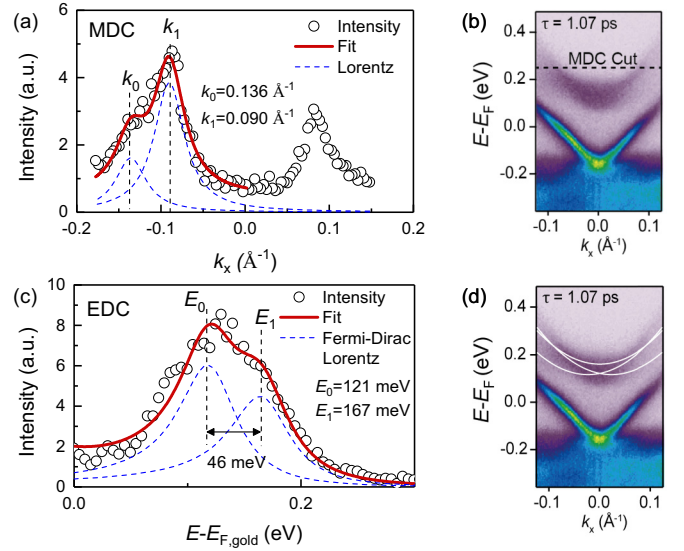

FIG. 4. The ARPES intensity distribution curves of 2DEG bands and band configuration. (a) Momentum distribution curve (MDC, black circles) measured at $E - E_F = 239.6$ meV when τ is 1.07 ps and the corresponding fit using two Lorentz oscillators (red solid line for the total fit, and blue dotted lines for each oscillator). (b) The black dotted line is the binding energy to obtain the MDC curve. (c) EDC (black circles) at Γ point and the corresponding fit using two Lorentz oscillators multiplied by the Fermi-Dirac distribution (red solid line for the total fit and blue dotted lines for each Lorentz oscillator). (d) The calculated 2DEG subbands with the Rashba-type band split (white lines) are overlapped with the experimental tr-ARPES results.

Having understood the formation of the Rashba split band in 2DEG, an interesting question is the role of the surface and internal bulk PV on the carrier dynamics of TSS and 2DEG near the surface. To address such a question, we have measured the low-energy conductivity using ultrafast THz spectroscopy [53,54]. Figure 5(a) shows the equilibrium THz conductivity of our sample. We fit our data by a multi-Drude-Fano model [55–57] (see Supplemental Material S6 [34]), where one Drude oscillator is responsible for the surface response (orange solid line), i.e., TSS or 2DEG, and another is for the bulk carrier response (black solid line). Because the TSS and 2DEG carriers are known to show a similar Drude weight and scattering rate [30,58], we consider that a single Drude oscillator is sufficient to describe both responses. On the other hand, the bulk response can be clearly separated from the surface response [59], in which there is a sixfold difference in the scattering rate and the corresponding line-shape difference (see Supplemental Material S6 [34] and Refs. [60,61] therein). Figures 5(b) and 5(c) show the optical pump-induced THz conductivity changes in the quasiequilibrium ($\tau = -20$ ps) and in the nonequilibrium ($\tau = 800$ ps) state, respectively. From the fits, we see that the the overall fit is less sensitive to the time-dependent changes of the bulk Drude part than the surface contribution. Although some part of the subtle details in the low frequency ($\sim$0.5 THz) range is not well explained by the fit, the bulk Drude response can be excluded for the origin of the measured photoinduced changes. At both delays, in addition, the spectra exhibit an
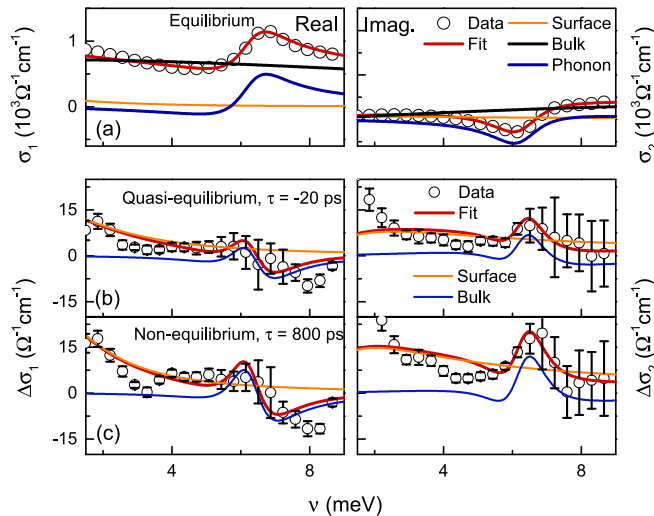
FIG. 5. The equilibrium THz conductivity and the pump-induced tr-THz conductivity changes. (a) Left: the real part $\sigma_1(\omega)$. Right: the imaginary part $\sigma_2(\omega)$. Red solid lines are fits (see Supplemental Material S6 [34]) using the surface Drude (orange solid line), bulk Drude (black solid line), and Fano-like oscillator (blue solid line). The surface Drude exhibits a scattering rate of $26 \, cm^{-1}$ and the bulk Drude exhibits a scattering rate of $150 \, cm^{-1}$. (b), (c) The measured optical conductivity changes (black circle) in the real part $\Delta\sigma_1(\omega)$ (left panel) and imaginary part $\Delta\sigma_2(\omega)$ (right panel) at a delay $\tau = -20 \, ps$ (b) and $\tau = 800 \, ps$ (c) after excitation. Red solid lines are fits (see Supplemental Material S6 [34]) using the differential changes of the surface Drude (orange solid line) and the bulk Drude (black solid line). The reference spectrum is the equilibrium conductivity in (a).

enhanced THz conductivity in both real and imaginary part, suggesting the increased surface charge density (orange solid line; see Supplemental Material S6 for the fitting details [34]). Interestingly, the increased surface charge density persists for a long time, i.e., τ from 800 ps (nonequilibrium state) to -20 ps (quasiequilibrium state). At first glance, the above THz observation seems to be contradictory to the tr-ARPES data [Figs. 2(c) and 2(e)]; tr-ARPES shows that the surface PV and the internal bulk PV are time dependent with an opposite direction. However, we note that the enhanced surface charge carrier density in the THz measurements stems from the surface charge accumulation in the downward band bending. In other words, we can understand that the TSS carrier dynamics due to the surface PV in the downward band bending are effective at any τ, while the shift of the TSS binding energy in the quasiequilibrium state originates from the internal bulk PV of the upward band bending. Although no energy shift of the TSS Fermi cutoff was observed in the tr-ARPES [Fig. 2(d)], it might be due to the broadened Fermi-Dirac distribution.

The THz experiments support that the increased surface charge density arises from the 2DEG, not from the bulk. Distinguishing the two is nontrivial in our tr-ARPES data alone. In the tr-ARPES data [Figs. 2(c) and 2(e) (red arrow)], the TSS binding energy exhibits dynamical shifts in an opposite direction depending on τ, while the quadratic band only shows the ARPES intensity enhancement. If the quadratic band is assigned to the bulk conduction band, the oscillator strength

of the bulk Drude in THz measurements (Fig. 5) should be increased both in the quasiequilibrium and nonequilibrium states. However, our experimental result demonstrates that only the oscillator strength of surface Drude is enhanced, and the change in the bulk Drude is negligible.

In conclusion, we have performed the time-resolved ARPES and THz measurements on *n*-type topological insulator Bi_2Te_3. The tr-ARPES results show that the internal bulk PV is dominant in the quasiequilibrium state over 4 μs, where the band bending is upward from the bulk to the TI surface. In the nonequilibrium state of a few 100's of ps, we found that the surface photovoltage is effective on the downward band bending. Ultrafast THz measurements reveal that carrier density of TSS and 2DEG increase in both nonequilibrium and quasiequilibrium states, which originates from the surface PV effect on the downward band bending. Compared to the prior experiments, where a monotonic band bending with a simple PV effect has been considered, our study indicates that there exists spatially distinct composite band bending. This enables the existence of 2DEG on *n*-type TIs with an upward band-bending configuration. Correspondingly, the spatially separated charges invoke the surface and internal bulk PV dynamics, where the former is effective on the downward band bending and the latter is dominant on the upward band bending.

[1] Y. L. Chen, J. G. Analytis, J. H. Chu, Z. K. Liu, S. K. Mo, X. L. Qi, H. J. Zhang, D. H. Lu, X. Dai, Z. Fang, S. C. Zhang, I. R. Fisher, Z. Hussain, and Z. X. Shen, Science **325**, 178 (2009).

[2] M. Z. Hasan and C. L. Kane, Rev. Mod. Phys. **82**, 3045 (2010).

[3] P. Roushan, J. Seo, C. V. Parker, Y. S. Hor, D. Hsieh, D. Qian, A. Richardella, M. Z. Hasan, R. J. Cava, and A. Yazdani, Nature (London) **460**, 1106 (2009).

[4] L. Fu and C. L. Kane, Phys. Rev. Lett. **100**, 096407 (2008).

[5] T. Shoman, A. Takayama, T. Sato, S. Souma, T. Takahashi, T. Oguchi, K. Segawa, and Y. Ando, Nat. Commun. **6**, 6547 (2015).

[6] K. J. A. Ooi and D. T. H. Tan, Proc. R. Soc. London, Ser. A **473**, 20170433 (2017).

[7] J. W. McIver, D. Hsieh, H. Steinberg, P. Jarillo-Herrero, and N. Gedik, Nat. Nanotechnol. **7**, 96 (2011).

[8] C. Kastl, C. Karnetzky, H. Karl, and A. W. Holleitner, Nat. Commun. **6**, 6617 (2015).

[9] Y. H. Wang, H. Steinberg, P. Jarillo-Herrero, and N. Gedik, Science **342**, 453 (2013).

[10] C.-M. Tu, Y.-C. Chen, P. Huang, P.-Y. Chuang, M.-Y. Lin, C.-M. Cheng, J.-Y. Lin, J.-Y. Juang, K.-H. Wu, and J.-C. A. Huang, Phys. Rev. B **96**, 195407 (2017).

[11] M. Brahlek, N. Koirala, N. Bansal, and S. Oh, Solid State Commun. **215-216**, 54 (2015).

[12] D. Galanakis and T. D. Stanescu, Phys. Rev. B **86**, 195311 (2012).

[13] L. Kronik and Y. Shapira, Surf. Sci. Rep. **37**, 1 (1999).

[14] Y. Ishida, T. Otsu, T. Shimada, M. Okawa, Y. Kobayashi, F. Iga, T. Takabatake, and S. Shin, Sci. Rep. **5**, 8160 (2015).

[15] M. Neupane, S. Y. Xu, Y. Ishida, S. Jia, B. M. Fregoso, C. Liu, I. Belopolski, G. Bian, N. Alidoust, T. Durakiewicz, V. Galitski, S. Shin, R. J. Cava, and M. Z. Hasan, Phys. Rev. Lett. **115**, 116801 (2015).

[16] E. Papalazarou, L. Khalil, M. Caputo, L. Perfetti, N. Nilforoushan, H. Deng, Z. Chen, S. Zhao, A. Taleb-Ibrahimi, M. Konczykowski, A. Hruban, A. Wołoś, A. Materna, L. Krusin-Elbaum, and M. Marsi, Phys. Rev. Mater. **2**, 104202 (2018).

[17] T. Yoshikawa, K. Sumida, Y. Ishida, J. Chen, M. Nurmamat, K. Akiba, A. Miyake, M. Tokunaga, K. A. Kokh, O. E. Tereshchenko, S. Shin, and A. Kimura, Phys. Rev. B **100**, 165311 (2019).

[18] T. Yoshikawa, Y. Ishida, K. Sumida, J. Chen, K. A. Kokh, O. E. Tereshchenko, S. Shin, and A. Kimura, Appl. Phys. Lett. **112**, 192104 (2018).

[19] S. Sim, H. Jang, N. Koirala, M. Brahlek, J. Moon, J. H. Sung, J. Park, S. Cha, S. Oh, M. H. Jo, J. H. Ahn, and H. Choi, Nat. Commun. **6**, 8814 (2015).

[20] Y. Wang, D. Zhu, Y. Wu, Y. Yang, J. Yu, R. Ramaswamy, R. Mishra, S. Shi, M. Elyasi, K. L. Teo, Y. Wu, and H. Yang, Nat. Commun. **8**, 1364 (2017).

[21] Y. Bai, F. Fei, S. Wang, N. Li, X. Li, F. Song, R. Li, Z. Xu, and P. Liu, Nat. Phys. **17**, 311 (2021).

[22] Y. H. Wang, D. Hsieh, E. J. Sie, H. Steinberg, D. R. Gardner, Y. S. Lee, P. Jarillo-Herrero, and N. Gedik, Phys. Rev. Lett. **109**, 127401 (2012).

[23] K. Sumida, Y. Ishida, T. Yoshikawa, J. Chen, M. Nurmamat, K. A. Kokh, O. E. Tereshchenko, S. Shin, and A. Kimura, Phys. Rev. B **99**, 085302 (2019).

[24] M. S. Bahramy, P. D. King, A. de la Torre, J. Chang, M. Shi, L. Patthey, G. Balakrishnan, P. Hofmann, R. Arita, N. Nagaosa, and F. Baumberger, Nat. Commun. **3**, 1159 (2012).

[25] M. Bianchi, D. Guan, S. Bao, J. Mi, B. B. Iversen, P. D. C. King, and P. Hofmann, Nat. Commun. **1**, 128 (2010).

[26] P. D. C. King, R. C. Hatch, M. Bianchi, R. Ovsyannikov, C. Lupulescu, G. Landolt, B. Slomski, J. H. Dil, D. Guan, J. L. Mi, E. D. L. Rienks, J. Fink, A. Lindblad, S. Svensson, S. Bao, G. Balakrishnan, B. B. Iversen, J. Osterwalder, W. Eberhardt, F. Baumberger, and P. Hofmann, Phys. Rev. Lett. **107**, 096802 (2011).

[27] M. Bianchi, R. C. Hatch, J. Mi, B. B. Iversen, and P. Hofmann, Phys. Rev. Lett. **107**, 086802 (2011).

[28] J. A. Sobota, S. Yang, J. G. Analytis, Y. L. Chen, I. R. Fisher, P. S. Kirchmann, and Z. X. Shen, Phys. Rev. Lett. **108**, 117403 (2012).

[29] A. Gauthier, J. A. Sobota, N. Gauthier, K.-J. Xu, H. Pfau, C. R. Rotundu, Z.-X. Shen, and P. S. Kirchmann, J. Appl. Phys. **128**, 093101 (2020).

[30] B. C. Park, T. H. Kim, K. I. Sim, B. Kang, J. W. Kim, B. Cho, K. H. Jeong, M. H. Cho, and J. H. Kim, Nat. Commun. **6**, 6552 (2015).

[31] L. Luo, X. Yang, X. Liu, Z. Liu, C. Vaswani, D. Cheng, M. Mootz, X. Zhao, Y. Yao, C. Z. Wang, K. M. Ho, I. E. Perakis, M. Dobrowolska, J. K. Furdyna, and J. Wang, Nat. Commun. **10**, 607 (2019).

[32] N. H. Jo, K. Lee, J. Kim, J. Jang, J. Kim, and M.-H. Jung, Appl. Phys. Lett. **104**, 252413 (2014).

[33] N. H. Jo, K. J. Lee, C. M. Kim, K. Okamoto, A. Kimura, K. Miyamoto, T. Okuda, Y. K. Kim, Z. Lee, T. Onimaru, T. Takabatake, and M. H. Jung, Phys. Rev. B **87**, 201105(R) (2013).

[34] See Supplemental Material at http://link.aps.org/supplemental/10.1103/PhysRevB.106.195430 for the additional experiment, calculation, and fitting details.

[35] Y. Ishida, T. Togashi, K. Yamamoto, M. Tanaka, T. Kiss, T. Otsu, Y. Kobayashi, and S. Shin, Rev. Sci. Instrum. **85**, 123904 (2014).

[36] C. W. Luo, H. J. Wang, S. A. Ku, H. J. Chen, T. T. Yeh, J. Y. Lin, K. H. Wu, J. Y. Juang, B. L. Young, T. Kobayashi, C. M. Cheng, C. H. Chen, K. D. Tsuei, R. Sankar, F. C. Chou, K. A. Kokh, O. E. Tereshchenko, E. V. Chulkov, Y. M. Andreev, and G. D. Gu, Nano Lett. **13**, 5797 (2013).

[37] S. Winnerl, M. Orlita, P. Plochocka, P. Kossacki, M. Potemski, T. Winzer, E. Malic, A. Knorr, M. Sprinkle, C. Berger, W. A. de Heer, H. Schneider, and M. Helm, Phys. Rev. Lett. **107**, 237401 (2011).

[38] D. Bröcker, T. Gießel, and W. Widdra, Chem. Phys. **299**, 247 (2004).

[39] J. M. Iannelli, J. Maserjian, B. R. Hancock, P. O. Andersson, and F. J. Grunthaner, Appl. Phys. Lett. **54**, 301 (1989).

[40] M. A. Romero, M. A. G. Martinez, and P. R. Herczfeld, IEEE Trans. Microwave Theory Tech. **44**, 2279 (1996).

[41] T. S. Moss, T. D. F. Hawkins, and G. J. Burrell, J. Phys. C: Solid State Phys. **1**, 1435 (1968).

[42] L. A. Coldren, S. W. Corzine, and M. L. Mašanović, in *Diode Lasers and Photonic Integrated Circuits* (John Wiley & Sons, Inc., New York, 2012), pp. 529–544.

[43] W. Richter and C. R. Becker, Phys. Status Solidi B **84**, 619 (1977).

[44] S. V. Eremeev, M. G. Vergniory, T. V. Menshchikova, A. A. Shaposhnikov, and E. V. Chulkov, New J. Phys. **14**, 113030 (2012).

[45] L. Cheng, C. La-o-vorakiat, C. S. Tang, S. K. Nair, B. Xia, L. Wang, J.-X. Zhu, and E. E. M. Chia, Appl. Phys. Lett. **104**, 211906 (2014).

[46] P. Di Pietro, N. Adhlakha, F. Piccirilli, A. Di Gaspare, J. Moon, S. Oh, S. Di Mitri, S. Spampinati, A. Perucchi, and S. Lupi, Phys. Rev. Lett. **124**, 226403 (2020).

[47] P. Dutta, D. Bhoi, A. Midya, N. Khan, P. Mandal, S. S. Samatham, and V. Ganesan, Appl. Phys. Lett. **100**, 251912 (2012).

[48] Y.-P. Lai, H.-J. Chen, K.-H. Wu, and J.-M. Liu, Appl. Phys. Lett. **105**, 232110 (2014).

[49] S. Moser, V. Jovic, R. Koch, L. Moreschini, J. S. Oh, C. Jozwiak, A. Bostwick, and E. Rotenberg, J. Electron Spectros. Relat. Phenom. **225**, 16 (2018).

[50] M. A. Toloza Sandoval, A. Ferreira da Silva, E. A. de Andrada e Silva, and G. C. La Rocca, Phys. Rev. B **83**, 235315 (2011).

[51] E. O. Kane, J. Phys. Chem. Solids **1**, 249 (1957).

[52] H. M. Benia, C. Lin, K. Kern, and C. R. Ast, Phys. Rev. Lett. **107**, 177602 (2011).

[53] S. Sim, M. Brahlek, N. Koirala, S. Cha, S. Oh, and H. Choi, Phys. Rev. B **89**, 165137 (2014).

[54] C. C. Homes, M. Reedyk, D. A. Cradles, and T. Timusk, Appl. Opt. **32**, 2976 (1993).

[55] S. Sim, N. Koirala, M. Brahlek, J. H. Sung, J. Park, S. Cha, M.-H. Jo, S. Oh, and H. Choi, Phys. Rev. B **91**, 235438 (2015).

[56] M. Dressel and G. Grüner, *Electrodynamics of Solids* (Cambridge University Press, Cambridge, UK, 2002).

[57] A. Damascelli, K. Schulte, D. vanderMarel, and A. A. Menovsky, Phys. Rev. B **55**, R4863(R) (1997).

[58] S. Chatterjee, T. Grunwald, D. Köhler, K. Pierz, D. Golde, M. Kira, and S. Koch, Phys. Status Solidi C **6**, 453 (2009).

[59] H. J. Park, B. C. Park, M.-C. Lee, D. W. Jeong, J. Park, J. S. Kim, H. S. Ji, J. H. Shim, K. W. Kim, S. J. Moon, H.-D. Kim, D.-Y. Cho, and T. W. Noh, Phys. Rev. B **96**, 155139 (2017).

[60] T. Hong, K. Choi, T. Ha, B. C. Park, K. I. Sim, J. H. Kim, J. H. Kim, J. E. Kwon, S. Lee, D. I. Kang, and H. H. Lee, J. Korean Phys. Soc. **64**, 727 (2014).

[61] D. Nakamura, Y. Imai, A. Maeda, and I. Tsukada, J. Phys. Soc. Jpn. **81**, 044709 (2012).